

# MozzaVID: Mozzarella Volumetric Image Dataset

Pawel Tomasz Pieta      Peter Winkel Rasmussen      Anders BJORHOLM DAHL  
 Jeppe Revall Frisvad      Siavash Bigdeli      Carsten Gundlach  
 Anders Nymark Christensen

{papi, pwra, abda, jerf, sarbi, cagu, anym}@dtu.dk  
 Technical University of Denmark, Kgs. Lyngby, Denmark

## Abstract

Influenced by the complexity of volumetric imaging, there is a shortage of established datasets useful for benchmarking volumetric deep-learning models. As a consequence, new and existing models are not easily comparable, limiting the development of architectures optimized specifically for volumetric data. To counteract this trend, we introduce *MozzaVID* – a large, clean, and versatile volumetric classification dataset. Our dataset contains X-ray computed tomography (CT) images of mozzarella microstructure and enables the classification of 25 cheese types and 149 cheese samples. We provide data in three different resolutions, resulting in three dataset instances containing from 591 to 37,824 images. While targeted for developing general purpose volumetric algorithms, the dataset also facilitates investigating the properties of mozzarella microstructure. The complex and disordered nature of food structures brings a unique challenge, where a choice of appropriate imaging method, scale, and sample size is not trivial. With this dataset, we aim to address these complexities, contributing to more robust structural analysis models and a deeper understanding of food structure. The dataset can be explored through: <https://papieta.github.io/MozzaVID/>

## 1. Introduction

Volumetric images reveal the internal shape and structure of objects, making them important for a wide range of fields such as medical imaging [20, 35, 77], material science [23, 57, 70], paleontology [14, 78] and food science [22, 73].

With the growing use of volumetric data, many image analysis algorithms have been developed to work well with this modality. Most notably, the versatility and power of deep learning methods have caused them to dominate research contributions, especially in the medical field [49, 66, 75, 95]. Together with this development, an interest in obtaining comprehensive, well-curated volumetric datasets [63, 65, 74, 83] has grown proportionally.

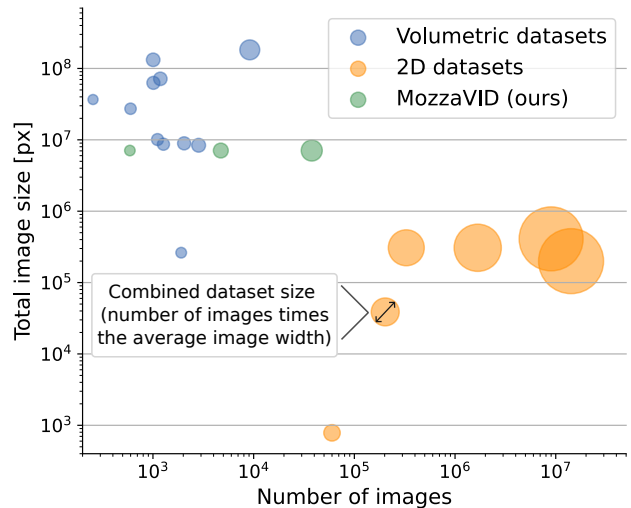


Figure 1. Comparison of typical volumetric and 2D dataset sizes. The three instances of the proposed *MozzaVID* dataset form a bridge between the two groups while maintaining the volume sizes known from other volumetric datasets. A complete overview of the visualized datasets can be found in Tabs. 1 and 2.

While the availability of volumetric datasets grows, their scope is still far from those known in 2D datasets. Volumetric imaging requires complex acquisition setups and typically generates few, very large image instances (between 1 and 100). Additionally, its most common area of use – medical research – poses further practical constraints on data collection and sharing [67]. As a result, the largest existing volumetric datasets are limited to a few moderately sized collections (containing between 100 and 10,000 volumes) [2, 3, 36, 62]. However, these bigger datasets usually target a complex scientific question that is difficult to address within a single deep-learning task. In contrast, even the smallest of widely recognized 2D datasets contain more than 60,000 images [17, 48, 51], and their primary objective is often to support general-purpose method development, which is reflected in their design.

In 2D model development, it has become a standard practice to evaluate proposed architectures on a set of benchmark datasets [21, 34, 52, 53, 71, 79, 90], demonstrating their versatility across different tasks. However, the limitations of existing volumetric datasets make it difficult to conduct similar evaluations. As a result, the most impactful contributions to the field tend to focus on adapting State-of-the-Art (SotA) 2D architectures to solve specific problems defined by a single dataset [12, 33, 80, 86, 91]. While this process can be effective at times, the properties of volumetric datasets make it likely that models optimized specifically for this modality may outperform those that were simply adapted from 2D [30, 43, 93, 94].

To facilitate the development and benchmarking of volumetric models, we introduce the mozzarella volumetric image dataset (MozzaVID). It consists of 591 synchrotron X-ray computed tomography (CT) scans of mozzarella cheese microstructure, enabling the classification of 25 cheeses and fine-grained classification of 149 samples. Mozzarella has an anisotropic microstructure that is highly disordered [5, 25], allowing for arbitrary splitting of the original scans with a low risk of introducing bias or losing crucial information. This property enables creating datasets with varying sample sizes and resolutions, which we demonstrate by proposing three dataset splits: containing 591, 4728, and 37,824 samples.

From a perspective of model performance indication, the generic, pattern-like nature of mozzarella microstructure allows it to serve as a supplement for scarce volumetric data. Many volumetric imaging targets in medical and material science share conceptual and visual similarities with mozzarella CT scans [1, 11, 27, 39, 42, 44, 72], and our experiments confirm that existing volumetric model performance trends are also present in the results on MozzaVID. With two classification targets and three dataset splits, MozzaVID supports evaluation across different levels of feature detail and varying data availability constraints. This positions MozzaVID as a dataset that bridges the gap between large, method-oriented 2D datasets and typical volumetric datasets, as shown in Fig. 1.

Apart from providing a general benchmark, the dataset is specifically targeted towards developing and evaluating methods for deep learning-based structural analysis. The structure of materials directly influences their functional properties, and structural analysis is an important use case for volumetric images [28, 41, 76]. At the same time, CT imaging has become a common choice for food analysis [26, 68, 84], where many products, such as meat, bread, pastries, and cheese (*e.g.* mozzarella) are heavily defined by their structural properties. With 34% of greenhouse gas emissions linked to food [13], understanding its structural properties is crucial for developing environmentally friendly alternatives to known structured foods that are also

pleasant to eat [6, 19, 29].

The microstructural variation of the MozzaVID samples is induced by a combination of the chemical composition and the processing parameters of the raw cheese curd. These parameters, along with rheological and functional measurements, form metadata, which will be published in a simplified form with the dataset.

The separation into cheese types and samples forms a hierarchy, where each cheese comprises 6 samples, with 4 scans performed within each sample, where the only difference between those is their spatial position. With this separation, we expect the samples to exhibit three levels of similarity: superficial similarity between samples produced with comparable recipes, moderate similarity between samples from the same cheese, and strong similarity between scans of the same sample.

Our experiments confirm the outlined relationships – with the biggest dataset instance we can obtain close to perfect classification of the 25 cheeses, as well as high accuracy on the 149 samples. By investigating the embeddings of the classifiers, we further show that they learn to arrange the classes into groups of cheese types with similar parameters and create a latent space that accurately covers the extent of the samples’ structural variation. This shows that through classification alone we can investigate and quantify the variability and relationships of the analyzed structures.

Our contributions can be summarized as follows:

- We introduce MozzaVID, a large and versatile dataset that bridges the gap between established 2D benchmark datasets and biggest volumetric datasets,
- We compare the performance of SoTA architectures on MozzaVID both in 2D and 3D, emphasizing the need for a specialized volumetric-oriented deep learning research,
- We explore the capabilities of MozzaVID in describing and explaining variability in mozzarella microstructure, highlighting its significance for deep learning-based structural analysis.

## 2. Related work

Volumetric datasets vary widely in imaging methods, sample sizes, and application domains. By far, the biggest and most diverse group consists of instances with a small volume count and no or limited annotation available. The goal of these datasets is a general analysis of the imaged object – either for domain-specific research or for advancing imaging technology. The two most notable mentions in this category are TomoBank [15] – a large repository of lab-scale and synchrotron CT datasets, and The Human Atlas project [18] – a repository of hierarchical phase-contrast CT of human organs.

Annotated volumetric datasets, particularly those targeted for deep learning applications, are predominantly found in the medical field. In this field, bigger datasets

Table 1. Existing biggest and most recognized volumetric datasets.

Dataset	# of volumes	Volume size	Primary application	Directly accessible	Task	# of labels
ADAM	254	512×512×140 (max)	Medical: brain MRI	No	Detection, segmentation	2
BraTS	50–2,040	240×240×155	Medical: brain MRI	No	Segmentation	4
KiTS	599	512×512×104	Medical: kidney CT	Yes	Segmentation, classification	3
LIDC-IDRI	1,010	512×512×(65–764)	Medical: thoracic CT	Yes	Detection, classification	2
MosMedData	1,110	512×512×(36–41)	Medical: chest CT	Yes	Segmentation, classification	5
CTSpine1k	1,005	512×512×(349–659)	Medical: spine CT	No	Segmentation	25
CTPelvic1k [50]	1,184	512×512×273 (mean)	Medical: pelvic CT	Yes	Segmentation	5
OASIS	2,842	256×256×128	Medical: brain MRI	No	Segmentation, classification	4
PN9	8,798	Not reported	Medical: thoracic CT	No	Detection	9
ATLAS v2.0 [47]	1,271	233×197×189	Medical: brain MRI	Yes	Segmentation	2
MedMNIST 3D	1,633–1,908	64×64×64	Method development	Yes	Classification	2/11
BugNIST	9,154 + 388	900×450/650×450/650	Method development	Yes	Detection under domain shift, classification	12
MozzaVID (ours)	591 to 37,824	192×192×192	Food science	Yes	Classification	25/149

Table 2. A subset of the most recognized 2D datasets as well as food-oriented 2D datasets.

Dataset	# of images	Image size	Primary application	Task
MNIST, Fashion-MNIST	60,000 (each)	28×28	Method testing	Classification
CelebA	202,599	178×218	Method development	Face attribute recognition, face recognition, face detection
COCO	~328,000	640×480	Method development	Object detection, keypoint detection, panoptic segmentation
ImageNet [16] (2014)	14,197,122	482×415	Computer vision	Object detection, image classification
Open Images [45]	~9,000,000	Unspecified	Computer vision	Object and visual relationship detection, instance segmentation
MSLS [85]	~1,680,000	480×640	Computer vision	Visual place recognition
FoodSeg103/152	7118/9490	Unspecified	Computer vision	Segmentation
Recipe1M+	13,000,000	Unspecified	Computer vision	Multimodal learning

are available for research in specific diagnostic areas, typically consisting of 100 to 1500 volumes. Frequently, these datasets are linked to a public challenge, demonstrated by well-recognized instances such as BraTS [3, 4, 63], KiTS [36, 37], or LIDC-IDRI/Luna16 [2, 74]. Despite being substantial by volumetric imaging standards, they are still relatively small for deep learning purposes. Notably, the PN9 dataset [62] provides a larger sample of 8798 lung CT scans. Outside the medical field, dataset availability is much more limited, with BugNIST [38] being a rare example, containing 9544 scans of common insects. A full overview of the biggest and most recognized volumetric datasets can be found in Tab. 1.

A majority of the existing datasets (especially those within the medical field) focus on segmentation or detection as the primary task. A smaller subset also offers classification targets (KiTS, MosMedData [64], OASIS [58]), often as an extension to the main target. MedMNIST 3D [92] and BugNIST are examples of large classification-oriented datasets. However, in the case of BugNIST, the baseline classification task is quite trivial, serving as a preliminary step before the main, domain shift task.

A significant limitation of many of the medical datasets is their accessibility [67]. Typically, medical data is rarely published due to confidentiality and de-identification constraints. Although this is not the case for the presented ex-

amples, many of them still cannot be directly downloaded online. Some require registering an account and/or agreeing to terms and conditions (BraTS, ADAM [81], OASIS), while others are only fully accessible after personally contacting the publisher (CTSpine1k [18], PN9).

From a methodological perspective, existing datasets pose further challenges. Many suffer from class imbalance, various sources of annotation and representation bias, as well as high specificity of the investigated problem, making them too constrained to serve as a generic baseline. Consequently, most volumetric deep learning research relies on unique, often case-specific datasets, limiting model generalizability and comparability across studies.

In context to presented characteristics, Tab. 2 lists a subset of the most recognized 2D datasets. In this summary, even the smallest of the datasets (MNIST [17], Fashion MNIST [88]) contain many more data instances than any of the existing volumetric counterparts. Importantly, many of these 2D datasets were made primarily for testing or development of new methods (MNIST, Fashion MNIST, CelebA [51], COCO [48]). This approach is further reflected in their design: through their simplicity, image size, curated setup, and clear task definition. Within this group, there is a notable representation of 2D food-focused datasets (FoodSeg103/152 [87], Recipe1M+ [59]), although they typically target food products and not food structure.

### 3. Data

The MozzaVID dataset consists of high-resolution CT images of 25 mozzarella cheese types with diverse functional properties. It is the first published instance of synchrotron-based CT imaging of mozzarella, providing detailed and high-quality images of its 3D microstructure.

#### 3.1. Acquisition and preprocessing

The anisotropic structure of mozzarella is created in the cooking-stretching step, where the cheese curd is heated and simultaneously kneaded with a rotating screw [24]. Investigated mozzarella types are made with varying cooking temperatures, speeds of the screw as well as optional additives. This experimental design is made to represent a set of realistic recipes and capture the range of potential structural variability of mozzarella. Importantly, three pairs of cheese were prepared with the same recipe, and the Cagliata cheese (class 25) was produced without stretching the curd, making it fully isotropic. Each cheese type was characterized with rheological and chemical measurements, enabling future structural analysis with detailed metadata (used in simplified form due to confidentiality). The samples were stored frozen and thawed directly before imaging.

Mozzarella cheese is a challenging target for CT imaging because its two primary components – proteins and fats have a similar, low X-ray attenuation coefficient, which results in prolonged scan times and sample thermal instability. Mozzarella can be scanned using laboratory micro-CT, but the resulting images are limited in number and very noisy [25]. A potential solution is to use a synchrotron X-ray light source. Although it is not applicable for routine data collection, it provides X-ray radiation of high flux and coherence, enabling fast scans at high resolution and low noise levels.

The measurements were conducted at the DanMAX beamline of the MAX IV synchrotron. Six samples were prepared from each cheese type by cutting out 1 cm cubes and wrapping them in parafilm, summing up to a total of 150 samples. Within each sample, four local tomography scans were taken, resulting in a total of 600 individual scans. All the scans were performed using the energy of 20 keV and exposure time of 1.5 ms. 2601 unique projections were taken at 0.55  $\mu\text{m}$  pixel size and 2356 $\times$ 2688 px resolution. The final scan width was approximately 1.3 mm. The scanning setup is introduced in Fig. 2.

Of the original reconstructed scans, 9 were discarded due to artefacts that heavily compromised image quality. In particular, a whole sample from cheese 4 was discarded, lowering the total number of samples to 149. The final set of 591 scans was cropped to the shape of 1601 $\times$ 1601 $\times$ 2156 (XYZ), and their histograms aligned by segmenting out the fat and protein and standardizing their intensities. This processed data was then treated as a raw input for the dataset.

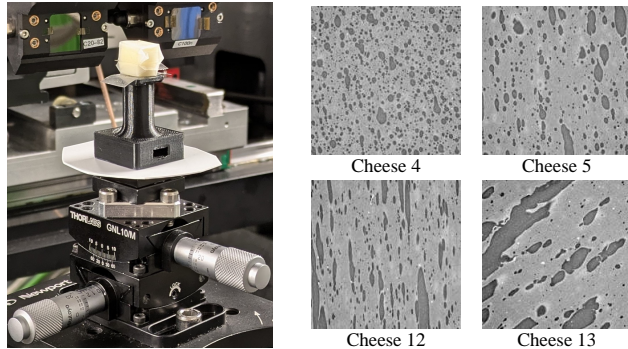


Figure 2. Mozzarella samples wrapped in parafilm and mounted for scanning (left). Structure variability demonstrated by 2D slices from four different cheese types (right). Light areas represent the protein matrix, while the dark areas are the fat globules/domains.

#### 3.2. Dataset preparation

The extracted raw scans (Fig. 2) present a detailed and clear description of the mozzarella structure, but their resolution is too high for most deep-learning algorithms. To address this issue, we propose a pipeline that downsamples the volumes and splits them to create more data instances. As previously mentioned, the internal structure of mozzarella does not contain specific macroscopic shapes or boundaries, allowing the samples to be split into smaller volumes without introducing bias. Additionally, the lack of repeating patterns or monotonous structures further minimizes the risk of ineffective splits. The practical limiting factors are the maximum split number and maximum effective pixel size – they need to be conservative enough to retain a meaningful representation of the structure. Excessive splitting could result in sub-volumes that are too small to describe relevant features, while excessive downsampling may lead to a loss of critical structural details.

Three main configurations of the dataset were prepared. Starting by limiting the volume size to a central cube of 1536 pixel width, the instances are then defined as:

1. **8X-1X (Small)** – each volume downsampled 8-fold, preserving the original count of 591 volumes,
2. **4X-2X (Base)** – each volume downsampled 4-fold and split into equal 8 sub-volumes (2 in each dimension), resulting in 4,728 volumes,
3. **2X-4X (Large)** – each volume downsampled 2-fold and split into 64 sub-volumes (4 in each dimension), resulting in 37,824 volumes.

The output resolution of all the configurations is standardized at 192  $\times$  192  $\times$  192 voxels. Fig. 3 illustrates the dataset preparation process.

We settle on the outlined approach as it is simple, creates volumes of manageable size, and aligns well with the goals of the dataset. The number of volumes in the Base and Large instances is well suited for the targets of 25



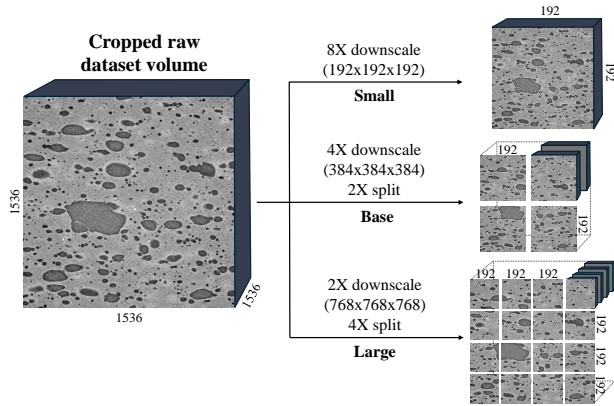


Figure 3. Sketch of the three proposed dataset configurations. The raw volume is downsampled and split, ensuring that in each case, the final volumes have the shape of 192 cubed.

and 149 classes respectively, while also enabling the exploration of the influence of scale on the accuracy. Although the Small instance is challenging for most non-trivial deep learning applications, it reflects the typical size of volumetric datasets, which rarely exceed this number. Consequently, potential volumetric methods have to be ready to address such a limitation.

## 4. Experiments

Within the proposed dataset, there is a hierarchy of targets and approaches that can be explored, forming three distinct ablation studies: classification granularity, dataset configuration, and dimensionality. These factors combine to form ten experimental setups that we evaluate on a set of benchmark architectures.

To assess the potential of classification in learning the space of possible mozzarella structures, we also investigate the embeddings of trained models and compare their distribution to the properties known from the experimental design of available cheese types.

### 4.1. Model selection and training setup

We selected five widely recognized model architectures within convolutional neural networks and transformers, to evaluate performance across the dataset variations. Due to the volume instance size (which roughly corresponds to a 2K RGB image) and subsequent memory limitations, most models are in their small/medium size version:

- **Convolutional Neural Networks (CNNs):**
  - *ResNet50* [34] – a standard benchmark model, sourced from TorchVision [56] and adapted to 3D by replacing 2D components (*e.g.* convolutions, pooling) with their 3D versions.
  - *MobileNetV2* [71] – an alternative lightweight model,

potentially fitting smaller volumetric datasets better. Chosen in the V2 version due to the availability of its 3D implementation at the 3D-CNN-PyTorch repository [55]. A 2D version was sourced from TorchVision.

- *ConvNeXt-S* [53] – a recent CNN architecture inspired by transformers. Sourced from the official repository and adapted to 3D in the same manner as ResNet50.

- **Transformers:**

- *ViT-B/16* [21] – a foundational vision transformer. Sourced from the vit-pytorch repository [82],
- *Swin-S* [52] – a hierarchical vision transformer that is more sensitive to multi-scale information. A 2D version was sourced from TorchVision, a 3D version was extracted from the components of SwinUNETR [33].

All models were trained using the AdamW optimizer [54] and an effective batch size of 32. The learning rate was fine-tuned for all models apart from the biggest 3D instances, where it was set to  $10^{-4}$  (details in the *Supplementary Material*). Data augmentation was limited to random flipping along the X and Y axes to preserve the spatial structure. All images are normalized using mean and standard deviation extracted from the raw data. The data is split into training, validation, and test sets with a fraction of 70%, 20%, and 10% respectively. We use cross-entropy loss for training and test set accuracy as the final performance evaluation metric. For each experimental setup, models were trained with an early stopping criterion based on validation loss. The CNNs were trained with a 30-epoch patience, while the transformer-based models, which generally converge more slowly, used a 50-epoch patience. If a model did not converge within a week, its training was stopped at the currently best result.

### 4.2. Ablation studies

#### 4.2.1 Granularity and dataset configuration

We evaluate two classification targets within the dataset: coarse-grain, corresponding to the 25 cheese types, and fine-grain, corresponding to the 149 individual cheese samples. For coarse-grain classification, we use all three dataset configurations: Small, Base, and Large. For fine-grain classification, only the Base and Large configurations are used. In the Small instance, the ratio of sample size to class number is too small.

#### 4.2.2 Dimensionality

To effectively investigate the influence of the volumetric representation, we compare models trained on full 3D volumes with those trained on 2D slices, simulating simpler imaging techniques, such as microscopy. In 2D imaging, the most accurate anisotropy measurements are obtained when the imaging plane is aligned parallel to the fiber direction, and in the case of mozzarella, this direction can be in-

ferred with the naked eye. In our dataset, due to the sample preparation, the fiber direction is always roughly perpendicular to the Z-axis. This means that Z-axis slices are an approximate representation of a 2D imaging approach. To provide a better overview of the structure in each volume, and fit to typical 3-channel 2D architectures, we choose three such slices from each volume: at 25%, 50%, and 75% of the height. For a fair comparison, no pre-trained weights are used on either 2D or 3D models.

### 4.3. Analysis of the learned representation

After training, we choose the best-performing model from the coarse-grained target and extract latent representations from its second-to-last layers. We then apply the UMAP [61] dimensionality reduction technique to investigate relationships between the clusters formed in this embedding space with the primary assumption being that the clusters will follow the class-based separation of the data.

Resulting UMAPs are then compared to the available metadata, specifically to the experimental design of investigated cheese types. This parameter space is first normalized and expressed with 2-component PCA (visualization in *Supplementary Material*), resulting in a spatial relationship between classes that can be compared to the UMAP of the clusters. If the models have learned a meaningful representation of the structure, embedding clusters representing similar cheese types should be located close to each other. To enable the visual comparison of UMAP clusters we assign a color representation to the points in the PCA space.

## 5. Results

### 5.1. Training

The majority of the models converged and reached the early stopping criterion, except for 3D Large instances of the ConvNeXt and Swin models, which continued to slowly improve until the predefined time limit. Models trained on the Small dataset exhibited strong overfitting to the training data, as expected given the dataset size, though it was partially mitigated through fine-tuning. Notably, the ResNet, MobileNet, and Swin models were the least affected.

Tab. 3 shows the complete classification results. Both the average and the per-model metrics demonstrate a significant improvement in accuracy with the 3D data. Interestingly, 3D models trained using the Coarse-Base setup consistently outperformed their counterparts trained on the 2D Large dataset. This suggests that even a smaller 3D dataset is more advantageous than a big 2D dataset for this problem. However, this trend is not visible in the fine-grained classification, indicating that in this task, the image resolution may play a more critical role than the 3D representation.

Across models, ResNet performed the most consistently in all the tasks and achieved the highest accuracy scores

for nearly all 3D configurations. MobileNetV2 also demonstrated stable performance, often achieving the highest accuracy among the 2D models. Swin provided a competitive but usually slightly worse performance across all cases, while ConvNeXt and ViT were performing the worst, showing significant variability across different configurations.

At a high level, top scores for both granularities (coarse-grained: 0.993, fine-grained: 0.935) confirm the validity and feasibility of the classification task. Both scores were only achieved on the Large dataset instance; fine-grained classification was much more challenging in the Base dataset (0.733), and coarse-grained was especially problematic in the Small dataset (0.860).

From the structural analysis perspective, the high accuracy achieved in the Large dataset suggests that even small volumes, approximately 0.2 mm in size, contain sufficient structural features for accurate classification of cheese types. At the same time, these volumes exhibit enough unique characteristics to identify them as part of a specific sample and its subtle, localized structural variations.

### 5.2. Learned representation

UMAP representation of the best-performing coarse-grained model shows distinct clustering of volumes corresponding to each class, with most classes forming tight, well-defined clusters (Fig. 4a). This clustering supports the high accuracy of the model, validating its ability to capture and distinguish between structural variations across classes.

Applying the PCA-based colormap (see *Supplementary Material*) provides additional insights into the UMAP representation (Fig. 4b). Classes 2, 7, 9, 10, 12, 18, and 24 form a large, central group of clusters with similar colors, suggesting the model has correctly identified their similarity. This group transitions to two additional groups: purple clusters on the top-right (classes 15, 22, 23) and green clusters on the bottom (classes 4, 17, 21). The color transition from red to green and red to purple aligns well with the spatial relationships present in the PCA space.

The positioning of some classes (13, 16, 19, and 20) deviates from the alignment with the PCA space, suggesting that the model’s representation may be coincidental or at least not very accurate. To evaluate this deviation, we use Fig. 4c, where the class clusters are substituted with example 2D slices of the volumetric data. This additional visualization highlights a strong similarity of cheese types located close to each other. Volumes on the right side of the map generally display anisotropic structures with large fat domains that grow even further toward the top. Conversely, the left and bottom areas contain volumes with smaller fats and potentially more isotropic structures. With this view, it is clear that the classes deemed problematic in the context of the cheese experimental design are positioned correctly in terms of their actual structural features.

Table 3. Classification accuracy of the trained models. The best results for each granularity are highlighted in bold, while the underline marks the best results in each experimental setup. Models marked with an asterisk did not converge within the time limit.

Granularity	Coarse						Fine			
	Small		Base		Large		Base		Large	
Split	2D	3D	2D	3D	2D	3D	2D	3D	2D	3D
ResNet50	0.480	<u>0.860</u>	0.781	<u>0.973</u>	0.932	<b>0.993</b>	<u>0.563</u>	0.683	0.770	<b>0.935</b>
MobileNetV2	0.480	0.760	<u>0.828</u>	0.964	<u>0.941</u>	0.963	0.514	<u>0.733</u>	<u>0.857</u>	0.895
ConvNeXt-S	0.440	0.500	0.566	0.805	0.750	0.936*	0.330	<u>0.733</u>	0.652	0.877*
ViT-B/16	0.260	0.300	0.421	0.819	0.731	0.927	0.235	0.541	0.442	0.855
Swin-S	<u>0.540</u>	0.720	0.697	0.941	0.929	0.976*	0.419	0.719	0.686	0.922*
Average	0.444	0.628	0.659	0.900	0.857	<b>0.959</b>	0.412	0.682	0.681	<b>0.905</b>

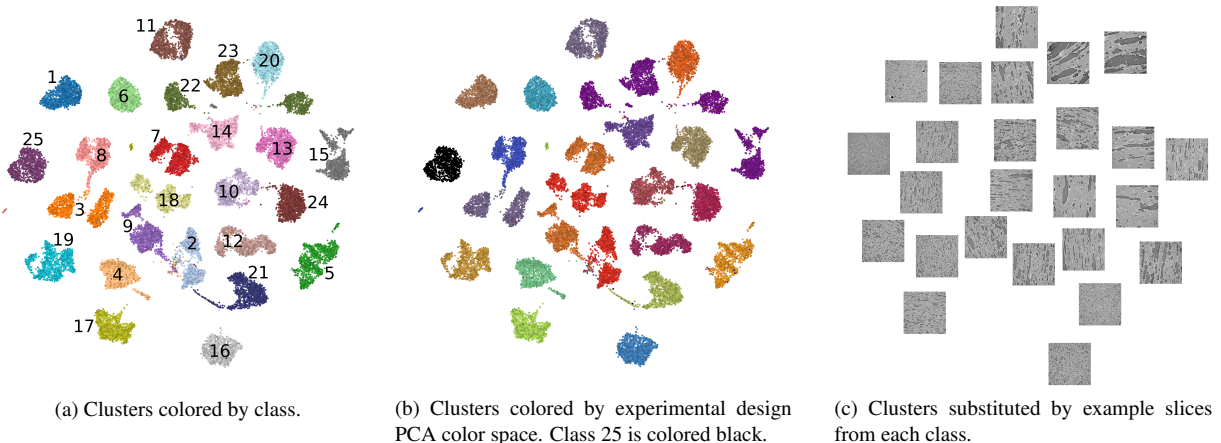


Figure 4. UMAP generated from second-to-last layer feature representations of the best-performing model in the coarse-grained classification task (ResNet50 trained on the Large dataset). Reduction parameters:  $n\_neighbors=15, min\_dist=0.5$ .

## 6. Discussion and Limitations

### 6.1. Data

The reliability of a dataset depends critically on the quality of its data sources, and the errors and noise that may arise at all stages of data generation. In the context of this study, these sources can be summarized into three groups: mozzarella cheese preparation, imaging, and post-processing.

Mozzarella production, as well as food production in general, cannot be fully controlled, resulting in variations in the final samples. These were highlighted in Sec. 5.2, where cheese types similar in terms of the experimental design had vastly different structures. While this discrepancy is interesting from a food science perspective, it has a negligible effect on dataset use in deep learning research.

All samples were prepared simultaneously and stored in similar conditions, excluding Cagliata cheese, which is one year older. With age, it developed multiple salt crystals, which then created very bright spots on the scans. This effect likely makes it easier to classify this cheese type but

does not compromise the overall dataset’s utility.

The power and coherence of synchrotron radiation allowed for generating low-noise and high-contrast scans, and the fast scanning time eliminated the risk of sample movement/deterioration during imaging. Post-processing steps were designed to limit the sources of bias and error, including discarding problematic scans, cropping volumes to avoid artifacts and inconsistencies near the scan edges, and normalizing voxel intensities across samples.

The orientation of the structure in the samples is also a potential source of bias. If two similar anisotropic structures are imaged with a consistent, different orientation, a model may learn to classify them based on this orientation alone. The issue is partially mitigated by the random flipping, as well as sample preparation, which involved cutting the samples in varying directions. However, it is not systematically addressed (*e.g.*, through random rotation offsets during reconstruction). To assess the potential impact of this issue, we conduct an additional rotation ablation study, detailed in the *Supplementary Material*. The results show

no evidence of orientation bias in the coarse-grained task and minor negative influence on the fine-grained task.

## 6.2. Experiments

The high accuracy scores achieved for both classification targets validate the problem’s feasibility but may also limit the potential for future improvement. However, the high scores apply only to the largest dataset instance, which is not representative of typical volumetric datasets. Reaching volume counts of over 10,000 will continue to be problematic for most volumetric imaging tasks, and the size of this dataset instance (37,760) is highly uncommon.

The classification accuracy drops significantly in the Base and Small instances that reflect more realistic conditions of volumetric datasets. This performance gap is the most prevalent trend in the training result, caused either by the general lack of data, or consequent overfitting to training data. We propose that future research could use the biggest instance to establish a base performance of a model, followed by a shift to the smaller data instances that are more challenging and representative of the typical volumetric task. For example, researchers could use the Small dataset with coarse-grained classes or the Base dataset with fine-grained classes.

The difference in performance between 2D and 3D models underscores the importance and impact of volumetric representation for this problem. Moreover, the strong performance of ResNet, as well as the discrepancy in MobileNet 2D and 3D results, suggest that simpler architectures continue to be the most effective for volumetric data. This further implies that some of the most advanced SotA models may be overly optimized for 2D images, limiting their effectiveness in volumetric tasks and presenting an opportunity to develop models specifically tailored for volumetric deep learning. Notably, the Swin model behavior reinforces this observation – despite the sensitivity of transformer architectures to dataset size [21, 46], it demonstrated surprisingly good performance on the Small and Base splits, making it a promising starting point for future research.

## 6.3. Classification as a method of structural analysis

While classification is a useful tool for high-level data analysis, it may not be the most direct approach for studying fine-grained structures. At the same time, many traditional image analysis methods are targeted specifically for texture and structure. However, some of these methods are very basic [31, 32], while others require careful parameter tuning and intensive computation [40, 69].

Through this classification task, we aim to explore the broad relationships and tendencies in mozzarella microstructure with implications for the analysis of structured foods. The disordered nature of food structures introduces significant uncertainty in any local measurements.

However, our results demonstrate that these local, irregular structures still retain enough distinctiveness to identify their properties both on the coarse and fine-grained levels. Future work will build on these findings by exploring alternative architectures, training setups, and representations that may further enhance the ability to capture and analyze these structural characteristics.

## 6.4. MozzaVID use as a benchmark

In MozzaVID we decide to focus on classification – mostly due to practical constraints of the data, as alternative targets would either be impossible or too trivial. This stands in contrast to many other datasets (Tabs. 1 and 2) that often focus on segmentation or include multiple prediction targets. While this could be seen as a limitation, it is also what lets us effectively perform the proposed data splits (Fig. 3) – a defining property of MozzaVID. Through these splits we are able to generate an unprecedented amount of volume samples, and to provide a complex fine-grained task with more classes than any existing volumetric dataset (Tab. 1). At the same time, classification remains the simplest, most fundamental task, enabling fast experimentation and more direct investigation of model performance.

An important observation emerges from comparing research trends in 2D and volumetric deep learning. Recent advancements in 2D model development suggest the superiority of transformer-based architectures [10, 21, 52, 60, 89], and there have been promising efforts to apply transformers for specific volumetric data [8, 9, 33, 91]. However, volumetric deep learning challenges continue to be dominated by more established convolution-based models [7, 37, 74]. This same trend is also evident in our experiments (Secs. 5 and 6.2), suggesting that future benchmarking results achieved on MozzaVID can serve as an indication of model performance across the field.

## 7. Conclusion

The MozzaVID dataset, with its substantial size and versatility, offers a flexible framework for volumetric model evaluation. By bridging the gap between established 2D benchmarks and existing volumetric datasets, MozzaVID facilitates the development of models tailored specifically for volumetric data. Models trained with MozzaVID provide valuable insights into the properties and patterns of mozzarella microstructure, setting the stage for more advanced structural analysis, both in mozzarella and other structured foods. The dataset can be explored through: <https://papieta.github.io/MozzaVID/>

**Acknowledgments:** This work was supported by Innovation Fund Denmark, project 0223-00041B (ExCheQuER). We acknowledge the MAX IV Laboratory for beamtime on the DanMAX beamline under proposal 20240276.



## References

- [1] Mariam Andersson, Hans Martin Kjer, Jonathan Rafael-Patino, Alexandra Pacureanu, Bente Pakkenberg, Jean-Philippe Thiran, Maurice Ptito, Martin Bech, Anders Bjorholm Dahl, Vedrana Andersen Dahl, and Tim B. Dyrby. Axon morphology is modulated by the local environment and impacts the noninvasive investigation of its structure–function relationship. *Proceedings of the National Academy of Sciences*, 117(52):33649–33659, 2020. 2
- [2] Samuel G. Armato, III, Geoffrey McLennan, Luc Bidaut, Michael F. McNitt-Gray, Charles R. Meyer, Anthony P. Reeves, Binsheng Zhao, Denise R. Aberle, Claudia I. Henschke, Eric A. Hoffman, Ella A. Kazerooni, Heber MacMahon, Edwin J. R. Van Beek, David Yankelevitz, Alberto M. Biancardi, Peyton H. Bland, Matthew S. Brown, Roger M. Engelmann, Gary E. Laderach, Daniel Max, Richard C. Pais, David P. Y. Qing, Rachael Y. Roberts, Amanda R. Smith, Adam Starkey, Poonam Batra, Philip Caligiuri, Ali Farooqi, Gregory W. Gladish, C. Matilda Jude, Reginald F. Munden, Iva Petkovska, Leslie E. Quint, Lawrence H. Schwartz, Baskaran Sundaram, Lori E. Dodd, Charles Fenimore, David Gur, Nicholas Petrick, John Freymann, Justin Kirby, Brian Hughes, Alessi Vande Castele, Sangeeta Gupte, Maha Sallam, Michael D. Heath, Michael H. Kuhn, Ekta Dharaiya, Richard Burns, David S. Fryd, Marcos Salganicoff, Vikram Anand, Uri Shreter, Stephen Vastagh, Barbara Y. Croft, and Laurence P. Clarke. Data from LIDC-IDRI. The Cancer Imaging Archive, 2015. 1, 3
- [3] Ujjwal Baid, Satyam Ghodasara, Suyash Mohan, Michel Bilello, Evan Calabrese, Errol Colak, Keyvan Farahani, Jayashree Kalpathy-Cramer, Felipe Campos Kitamura, Sarthak Pati, Luciano Prevedello, Jeffrey Rudie, Chiharu Sako, Russell Shinohara, Timothy Bergquist, Rong Chai, James Eddy, Julia Elliott, Walter Reade, Thomas Schaffter, Thomas Yu, Jiaxin Zheng, Christos Davatzikos, John Mongan, Christopher Hess, Soonmee Cha, Javier Villanueva-Meyer, John B. Freymann, Justin S. Kirby, Benedikt Wiestler, Priscila Crivellaro, Rivka R. Colen, Aikaterini Kotrotsou, Daniel Marcus, Mikhail Milchenko, Arash Nazeri, Hassan Fathallah-Shaykh, Roland Wiest, Andras Jakab, Marc-André Weber, Abhishek Mahajan, Bjoern Menze, Adam E. Flanders, and Spyridon Bakas. RSNA-ASNR-MICCAI-BraTS-2021, 2023. 1, 3
- [4] Spyridon Bakas, Hamed Akbari, Aristeidis Sotiras, Michel Bilello, Martin Rozycki, Justin S. Kirby, John B. Freymann, Keyvan Farahani, and Christos Davatzikos. Advancing the cancer genome atlas glioma MRI collections with expert segmentation labels and radiomic features. *Scientific Data*, 4(1):170117, 2017. 3
- [5] Ramona Bast, Prateek Sharma, Hannah K. B. Easton, Tzvetelin T. Dessev, Mita Lad, and Peter A. Munro. Tensile testing to quantitate the anisotropy and strain hardening of mozzarella cheese. *International Dairy Journal*, 44:6–14, 2015. 2
- [6] Zuhaib Fayaz Bhat and Hina Fayaz. Prospectus of cultured meat - advancing meat alternatives. *Journal of Food Science and Technology*, 48(2):125–140, 2011. 2
- [7] Patrick Bilic, Patrick Christ, Hongwei Bran Li, Eugene Vorontsov, Avi Ben-Cohen, Georgios Kaissis, Adi Szeskin, Colin Jacobs, Gabriel Efrain Humpire Mamani, Gabriel Chartrand, Fabian Lohöfer, Julian Walter Holch, Wieland Sommer, Felix Hofmann, Alexandre Hostettler, Naama Lev-Cohain, Michal Drozdal, Michal Marianne Amitai, Rafael Vivanti, Jacob Sosna, Ivan Ezhov, Anjany Sekuboyina, Fernando Navarro, Florian Kofler, Johannes C. Paetzold, Suprosanna Shit, Xiaobin Hu, Jana Lipková, Markus Rempfler, Marie Piraud, Jan Kirschke, Benedikt Wiestler, Zhiheng Zhang, Christian Hülsemeyer, Marcel Beetz, Florian Ettliger, Michela Antonelli, Woong Bae, Míriam Beller, Lei Bi, Hao Chen, Grzegorz Chlebus, Erik B. Dam, Qi Dou, Chi Wing Fu, Bogdan Georgescu, Xavier Giró-i Nieto, Felix Gruen, Xu Han, Pheng Ann Heng, Jürgen Hesser, Jan Hendrik Moltz, Christian Igel, Fabian Isensee, Paul Jäger, Fucang Jia, Krishna Chaitanya Kaluva, Mahendra Khened, Ildoo Kim, Jae Hun Kim, Sungwoong Kim, Simon Kohl, Tomasz Konopczynski, Avinash Kori, Ganapathy Krishnamurthi, Fan Li, Hongchao Li, Junbo Li, Xiaomeng Li, John Lowengrub, Jun Ma, Klaus Maier-Hein, Kevis Kokitsi Maninis, Hans Meine, Dorit Merhof, Akshay Pai, Mathias Perslev, Jens Petersen, Jordi Pont-Tuset, Jin Qi, Xiaojuan Qi, Oliver Rippel, Karsten Roth, Ignacio Sarasua, Andrea Schenk, Zengming Shen, Jordi Torres, Christian Wachinger, Chunliang Wang, Leon Wenginger, Jianrong Wu, Daguang Xu, Xiaoping Yang, Simon Chun Ho Yu, Yading Yuan, Miao Yue, Liping Zhang, Jorge Cardoso, Spyridon Bakas, Rickmer Braren, Volker Heinemann, Christopher Pal, An Tang, Samuel Kadoury, Luc Soler, Bram van Ginneken, Hayit Greenspan, Leo Joskowicz, and Bjoern Menze. The liver tumor segmentation benchmark (LiTS). *Medical Image Analysis*, 84:102680, 2023. 8
- [8] Junyu Chen, Yufan He, Eric Frey, Ye Li, and Yong Du. ViT-V-Net: Vision transformer for unsupervised volumetric medical image registration. In *Medical Imaging with Deep Learning*, 2021. 8
- [9] Jieneng Chen, Jieru Mei, Xianhang Li, Yongyi Lu, Qihang Yu, Qingyue Wei, Xiangde Luo, Yutong Xie, Ehsan Adeli, Yan Wang, Matthew P. Lungren, Shaoting Zhang, Lei Xing, Le Lu, Alan Yuille, and Yuyin Zhou. TransUNet: rethinking the u-net architecture design for medical image segmentation through the lens of transformers. *Medical Image Analysis*, 97:103280, 2024. 8
- [10] Bowen Cheng, Ishan Misra, Alexander G. Schwing, Alexander Kirillov, and Rohit Girdhar. Masked-attention mask transformer for universal image segmentation. *Proceedings of the Ieee Computer Society Conference on Computer Vision and Pattern Recognition*, 2022-:1280–1289, 2022. 8
- [11] Patrik Christen, Keita Ito, Frietson Galis, and Bert van Rietbergen. Determination of hip-joint loading patterns of living and extinct mammals using an inverse Wolff’s law approach. *Biomechanics and Modeling in Mechanobiology*, 14(2):427–432, 2015. 2
- [12] Özgün Çiçek, Ahmed Abdulkadir, Soeren S. Lienkamp, Thomas Brox, and Olaf Ronneberger. 3D U-Net: Learning dense volumetric segmentation from sparse annotation. In *Medical Image Computing and Computer-Assisted Inter-*

- vention (MICCAI 2016), pages 424–432. Lecture Notes in Computer Science, Vol. 9901. Springer, 2016. 2
- [13] M. Crippa, E. Solazzo, D. Guizzardi, F. Monforti-Ferrario, F. N. Tubiello, and A. Leip. Food systems are responsible for a third of global anthropogenic GHG emissions. *Nature Food*, 2(3):198–209, 2021. 2
- [14] John A. Cunningham, Imran A. Rahman, Stephan Lautenschlager, Emily J. Rayfield, and Philip C. J. Donoghue. A virtual world of paleontology. *Trends in Ecology and Evolution*, 29(6):347–357, 2014. 1
- [15] Francesco De Carlo, Doğa Gürsoy, Daniel J. Ching, K. Joost Batenburg, Wolfgang Ludwig, Lucia Mancini, Federica Marone, Rajmund Mokso, Daniël M. Pelt, Jan Sijbers, and Mark Rivers. TomoBank: A tomographic data repository for computational x-ray science. *Measurement Science and Technology*, 29(3):034004, 2018. 2
- [16] Jia Deng, Wei Dong, Richard Socher, Li-Jia Li, Kai Li, and Li Fei-Fei. ImageNet: A large-scale hierarchical image database. In *Proceedings of Computer Vision and Pattern Recognition (CVPR)*. IEEE, 2009. 3
- [17] Li Deng. The MNIST database of handwritten digit images for machine learning research [best of the web]. *IEEE Signal Processing Magazine*, 29(6):141–142, 2012. 1, 3
- [18] Yang Deng, Ce Wang, Yuan Hui, Qian Li, Jun Li, Shiwei Luo, Mengke Sun, Quan Quan, Shuxin Yang, You Hao, Pengbo Liu, Honghu Xiao, Chunpeng Zhao, Xinbao Wu, and S. Kevin Zhou. CTSpine1K: A large-scale dataset for spinal vertebrae segmentation in computed tomography. arXiv:2105.14711 [eess.IV], 2024. 2, 3
- [19] S. Dobson and A. G. Marangoni. Methodology and development of a high-protein plant-based cheese alternative. *Current Research in Food Science*, 7:100632, 2023. 2
- [20] Kunio Doi. Computer-aided diagnosis in medical imaging: Historical review, current status and future potential. *Computerized Medical Imaging and Graphics*, 31(4-5):198–211, 2007. 1
- [21] Alexey Dosovitskiy, Lucas Beyer, Alexander Kolesnikov, Dirk Weissenborn, Xiaohua Zhai, Thomas Unterthiner, Mostafa Dehghani, Matthias Minderer, Georg Heigold, Sylvain Gelly, Jakob Szepesvári, and Neil Houlsby. An image is worth 16x16 words: Transformers for image recognition at scale. *Iclr 2021 - 9th International Conference on Learning Representations*, 2021. 2, 5, 8
- [22] Zhe Du, Yongguang Hu, Noman Ali Buttar, and Ashraf Mahmood. X-ray computed tomography for quality inspection of agricultural products: A review. *Food Science & Nutrition*, 7(10):3146–3160, 2019. 1
- [23] Anton du Plessis and William P. Boshoff. A review of X-ray computed tomography of concrete and asphalt construction materials. *Construction and Building Materials*, 199:637–651, 2019. 1
- [24] Ran Feng, Sylvain Barjon, Frans W. J. van den Berg, Søren Kristian Lillevang, and Lilia Ahrné. Effect of residence time in the cooker-stretcher on mozzarella cheese composition, structure and functionality. *Journal of Food Engineering*, 309:110690, 2021. 4
- [25] Ran Feng, Franciscus Winfried J. van der Berg, Rajmund Mokso, Søren Kristian Lillevang, and Lilia Ahrné. Structural, rheological and functional properties of extruded mozzarella cheese influenced by the properties of the renneted casein gels. *Food Hydrocolloids*, 137:108322, 2023. 2, 4
- [26] P. Frisullo, J. Laverse, R. Marino, and M.A. Del Nobile. X-ray computed tomography to study processed meat microstructure. *Journal of Food Engineering*, 94(3–4):283–289, 2009. 2
- [27] Yantao Gao, Wenfeng Hu, Sanfa Xin, and Lijuan Sun. A review of applications of CT imaging on fiber reinforced composites. *Journal of Composite Materials*, 56(1):133–164, 2022. 2
- [28] S. C. Garcea, Y. Wang, and P. J. Withers. X-ray computed tomography of polymer composites. *Composites Science and Technology*, 156:305–319, 2018. 2
- [29] Fernanda C. Godoi, Sangeeta Prakash, and Bhesh R. Bhandari. 3D printing technologies applied for food design: Status and prospects. *Journal of Food Engineering*, 179:44–54, 2016. 2
- [30] Benjamin Graham, Martin Engelcke, and Laurens Van Der Maaten. 3D semantic segmentation with submanifold sparse convolutional networks. *Proceedings of Computer Vision and Pattern Recognition (CVPR)*, pages 9224–9232, 2018. 2
- [31] Goesta H. Granlund. In search of a general picture processing operator. *Computer Graphics and Image Processing*, 8(2):155–173, 1978. 8
- [32] Robert M. Haralick, Karthikeyan Shanmugam, and Its’Hak Dinstein. Textural features for image classification. *IEEE Transactions on Systems, Man, and Cybernetics*, SMC3(6):610–621, 1973. 8
- [33] Ali Hatamizadeh, Vishwesh Nath, Yucheng Tang, Dong Yang, Holger R. Roth, and Daguang Xu. Swin UNETR: Swin transformers for semantic segmentation of brain tumors in MRI images. In *Brainlesion: Glioma, Multiple Sclerosis, Stroke and Traumatic Brain Injuries (BrainLes 2021)*, pages 272–284. Lecture Notes in Computer Science, Vol. 12962. Springer, 2022. 2, 5, 8
- [34] Kaiming He, Xiangyu Zhang, Shaoqing Ren, and Jian Sun. Deep residual learning for image recognition. In *Proceedings of Computer Vision and Pattern Recognition (CVPR)*, pages 770–778. IEEE, 2016. 2, 5
- [35] Tobias Heimann and Hans Peter Meinzer. Statistical shape models for 3D medical image segmentation: A review. *Medical Image Analysis*, 13(4):543–563, 2009. 1
- [36] Nicholas Heller, Niranjan Sathianathan, Arveen Kalapara, Edward Walczak, Keenan Moore, Heather Kaluzniak, Joel Rosenberg, Paul Blake, Zachary Rengel, Makinna Oestreich, Joshua Dean, Michael Tradewell, Aneri Shah, Resha Tejpal, Zachary Edgerton, Matthew Peterson, Shaneabas Raza, Subodh Regmi, Nikolaos Papanikolopoulos, and Christopher Weight. The KiTS19 challenge data: 300 kidney tumor cases with clinical context, CT semantic segmentations, and surgical outcomes. arXiv:1904.00445 [q-bio.QM], 2020. 1, 3
- [37] Nicholas Heller, Fabian Isensee, Klaus H. Maier-Hein, Xiaoshuai Hou, Chunmei Xie, Fengyi Li, Yang Nan, Guangrui

- Mu, Zhiyong Lin, Miofei Han, Guang Yao, Yaozong Gao, Yao Zhang, Yixin Wang, Feng Hou, Jiawei Yang, Guangwei Xiong, Jiang Tian, Cheng Zhong, Jun Ma, Jack Rickman, Joshua Dean, Bethany Stai, Resha Tejpal, Makinna Oestreich, Paul Blake, Heather Kaluzniak, Shaneabbas Raza, Joel Rosenberg, Keenan Moore, Edward Walczak, Zachary Rengel, Zach Edgerton, Ranveer Vasdev, Matthew Peterson, Sean McSweeney, Sarah Peterson, Arveen Kalapara, Niranjan Sathianathen, Nikolaos Papanikolopoulos, and Christopher Weight. The state of the art in kidney and kidney tumor segmentation in contrast-enhanced CT imaging: Results of the KiTS19 challenge. *Medical Image Analysis*, 67:101821, 2021. 3, 8
- [38] Patrick Møller Jensen, Vedrana Andersen Dahl, Rebecca Engberg, Carsten Gundlach, Hans Marin Kjer, and Anders Bjorholm Dahl. BugNIST a large volumetric dataset for object detection under domain shift. *Proceedings of the 18th European Conference on Computer Vision – Eccv 2024*, 15090:18–36, 2025. 3
- [39] Niels Jeppesen, Anders N. Christensen, Vedrana A. Dahl, and Anders B. Dahl. Sparse layered graphs for multi-object segmentation. In *Proceedings of Computer Vision and Pattern Recognition (CVPR)*, pages 12774–12782. IEEE, 2020. 2
- [40] N. Jeppesen, L. P. Mikkelsen, A. B. Dahl, A. N. Christensen, and V. A. Dahl. Quantifying effects of manufacturing methods on fiber orientation in unidirectional composites using structure tensor analysis. *Composites Part A: Applied Science and Manufacturing*, 149:106541, 2021. 8
- [41] Radmir Karamov, Luca M. Martulli, Martin Kerschbaum, Ivan Sergeichev, Yentl Swolfs, and Stepan V. Lomov. Micro-CT based structure tensor analysis of fibre orientation in random fibre composites versus high-fidelity fibre identification methods. *Composite Structures*, 235:111818, 2020. 2
- [42] Özgür Keleş, Eric H. Anderson, Jimmy Huynh, Jeff Gelb, Jouni Freund, and Alp Karakoç. Stochastic fracture of additively manufactured porous composites. *Scientific Reports*, 8(1):15437, 2018. 2
- [43] Doyub Kim, Minjae Lee, and Ken Museth. NeuralVDB: High-resolution sparse volume representation using hierarchical neural networks. *ACM Transactions on Graphics*, 43(2):20, 2024. 2
- [44] Subok Kim, Sanghun Jang, and Onseok Lee. Muscle structure assessment using synchrotron radiation x-ray micro-computed tomography in murine with cerebral ischemia. *Scientific Reports*, 14(1):26825, 2024. 2
- [45] Alina Kuznetsova, Hassan Rom, Neil Alldrin, Jasper Uijlings, Ivan Krasin, Jordi Pont-Tuset, Shahab Kamali, Stefan Popov, Matteo Mallocci, Alexander Kolesnikov, Tom Duerig, and Vittorio Ferrari. The open images dataset V4: Unified image classification, object detection, and visual relationship detection at scale. *International Journal of Computer Vision*, 128(7):1956–1981, 2020. 3
- [46] Seung Hoon Lee, Seunghyun Lee, and Byung Cheol Song. Vision transformer for small-size datasets, 2021. 8
- [47] Sook-Lei Liew, Bethany P. Lo, Miranda R. Donnelly, Artemis Zavaliangos-Petropulu, Jessica N. Jeong, Giuseppe Barisano, Alexandre Hutton, Julia P. Simon, Julia M. Juliano, Anisha Suri, Zhizhuo Wang, Aisha Abdullah, Jun Kim, Tyler Ard, Nerisa Banaj, Michael R. Borich, Lara A. Boyd, Amy Brodtmann, Cathrin M. Buetefisch, Lei Cao, Jessica M. Cassidy, Valentina Ciullo, Adriana B. Conforto, Steven C. Cramer, Rosalia Dacosta-Aguayo, Ezequiel de la Rosa, Martin Domin, Adrienne N. Dula, Wuwei Feng, Alexandre R. Franco, Fatemeh Geranmayeh, Alexandre Gramfort, Chris M. Gregory, Colleen A. Hanlon, Brenton G. Hordacre, Steven A. Kautz, Mohamed Salah Khelif, Hosung Kim, Jan S. Kirschke, Jingchun Liu, Martin Lotze, Bradley J. MacIntosh, Maria Mataró, Feroze B. Mohamed, Jan E. Nordvik, Gilsoon Park, Amy Pienta, Fabrizio Piras, Shane M. Redman, Kate P. Revill, Mauricio Reyes, Andrew D. Robertson, Na Jin Seo, Surjo R. Soekadar, Gianfranco Spalletta, Alison Sweet, Maria Telenczuk, Gregory Thielman, Lars T. Westlye, Carolee J. Winstein, George F. Wittenberg, Kristin A. Wong, and Chunshui Yu. A large, curated, open-source stroke neuroimaging dataset to improve lesion segmentation algorithms. *Scientific Data*, 9:320, 2022. 3
- [48] Tsung Yi Lin, Michael Maire, Serge Belongie, James Hays, Pietro Perona, Deva Ramanan, Piotr Dollár, and C. Lawrence Zitnick. Microsoft COCO: Common objects in context. *Lecture Notes in Computer Science (including Subseries Lecture Notes in Artificial Intelligence and Lecture Notes in Bioinformatics)*, 8693(5):740–755, 2014. 1, 3
- [49] Geert Litjens, Thijs Kooi, Babak Ehteshami Bejnordi, Arnaud Arindra Adiyoso Setio, Francesco Ciompi, Mohsen Ghafoorian, Jeroen A. W. M. van der Laak, Bram van Ginneken, and Clara I. Sánchez. A survey on deep learning in medical image analysis. *Medical Image Analysis*, 42:60–88, 2017. 1
- [50] Pengbo Liu, Hu Han, Yuanqi Du, Heqin Zhu, Yinhao Li, Feng Gu, Honghu Xiao, Jun Li, Chunpeng Zhao, Li Xiao, Xinbao Wu, and S. Kevin Zhou. Deep Learning to Segment Pelvic Bones: Large-scale CT Datasets and Baseline Models, 2021. 3
- [51] Ziwei Liu, Ping Luo, Xiaogang Wang, and Xiaoou Tang. Deep learning face attributes in the wild. In *Proceedings of International Conference on Computer Vision (ICCV)*, pages 3730–3738. IEEE, 2015. 1, 3
- [52] Ze Liu, Yutong Lin, Yue Cao, Han Hu, Yixuan Wei, Zheng Zhang, Stephen Lin, and Baining Guo. Swin transformer: Hierarchical vision transformer using shifted windows. *Proceedings of International Conference on Computer Vision (ICCV)*, pages 9992–10002, 2021. 2, 5, 8
- [53] Zhuang Liu, Hanzi Mao, Chao Yuan Wu, Christoph Feichtenhofer, Trevor Darrell, and Saining Xie. A ConvNet for the 2020s. In *Proceedings of Computer Vision and Pattern Recognition (CVPR)*, pages 11966–11976. IEEE, 2022. 2, 5
- [54] Ilya Loshchilov and Frank Hutter. Decoupled weight decay regularization. *7th International Conference on Learning Representations, ICLR 2019*, 2019. 5
- [55] 3D-CNN-PyTorch maintainers and contributors. 3D-CNN-PyTorch: PyTorch implementation for 3dCNNs for medical images. <https://github.com/xmuyzz/3D-CNN-PyTorch>, 2022. 5



- [56] TorchVision maintainers and contributors. TorchVision: PyTorch’s computer vision library. <https://github.com/pytorch/vision>, 2016. 5
- [57] E. Maire and P. J. Withers. Quantitative X-ray tomography. *International Materials Reviews*, 59(1):1–43, 2014. 1
- [58] Daniel S. Marcus, Tracy H. Wang, Jamie Parker, John G. Csernansky, John C. Morris, and Randy L. Buckner. Open access series of imaging studies (OASIS): Cross-sectional MRI data in young, middle aged, nondemented, and demented older adults. *Journal of Cognitive Neuroscience*, 19(9):1498–1507, 2007. 3
- [59] Javier Marin, Aritro Biswas, Ferda Ofli, Nicholas Hynes, Amaia Salvador, Yusuf Aytar, Ingmar Weber, and Antonio Torralba. Recipe1m+: A dataset for learning cross-modal embeddings for cooking recipes and food images. *IEEE Transactions on Pattern Analysis and Machine Intelligence*, 43(1):187–203, 2021. 3
- [60] José Maurício, Inês Domingues, and Jorge Bernardino. Comparing vision transformers and convolutional neural networks for image classification: A literature review. *Applied Sciences (switzerland)*, 13(9):5521, 2023. 8
- [61] Leland McInnes, John Healy, Nathaniel Saul, and Lukas Großberger. UMAP: Uniform manifold approximation and projection. *Journal of Open Source Software*, 3(29):861, 2018. 6
- [62] Jie Mei, Ming-Ming Cheng, Gang Xu, Lan-Ruo Wan, and Huan Zhang. SANet: A slice-aware network for pulmonary nodule detection. *IEEE Transactions on Pattern Analysis and Machine Intelligence*, 44(8):4374–4387, 2021. 1, 3
- [63] Bjoern H. Menze, Andras Jakab, Stefan Bauer, Jayashree Kalpathy-Cramer, Keyvan Farahani, Justin Kirby, Yuliya Burren, Nicole Porz, Johannes Slotboom, Roland Wiest, Levente Lenczi, Elizabeth Gerstner, Marc-Andre Weber, Tal Arbel, Brian B. Avants, Nicholas Ayache, Patricia Buendia, D. Louis Collins, Nicolas Cordier, Jason J. Corso, Antonio Criminisi, Tilak Das, Herve Delingette, Cagatay Demiralp, Christopher R. Durst, Michel Dojat, Senan Doyle, Joana Festa, Florence Forbes, Ezequiel Geremia, Ben Glocker, Polina Golland, Xiaotao Guo, Andac Hamamci, Khan M. Iftekharuddin, Raj Jena, Nigel M. John, Ender Konukoglu, Danial Lashkari, Jose Antonio Mariz, Raphael Meier, Sergio Pereira, Doina Precup, Stephen J. Price, Tammy Riklin Raviv, Syed M. S. Reza, Michael Ryan, Duygu Sarikaya, Lawrence Schwartz, Hoo-Chang Shin, Jamie Shotton, Carlos A. Silva, Nuno Sousa, Nagesh K. Subbanna, Gabor Szekely, Thomas J. Taylor, Owen M. Thomas, Nicholas J. Tustison, Gozde Unal, Flor Vasseur, Max Wintermark, Dong Hye Ye, Liang Zhao, Binsheng Zhao, Darko Zikic, Marcel Prastawa, Mauricio Reyes, and Koen Van Leemput. The multimodal brain tumor image segmentation benchmark (BRATS). *IEEE Transactions on Medical Imaging*, 34(10):1993–2024, 2015. 1, 3
- [64] Sergey P. Morozov, Anna E. Andreychenko, Ivan A. Blokhin, Pavel B. Gelezhe, Anna P. Gonchar, Alexander E. Nikolaev, Nikolay A. Pavlov, Valeria Yu. Chernina, and Victor A. Gombolevskiy. MosMedData: data set of 1110 chest CT scans performed during the covid-19 epidemic. *Digital Diagnostics*, 1(1):49–59, 2020. 3
- [65] Tiago Mota, M. Rita Verdelho, Diogo J. Araújo, Alceu Bisoto, Carlos Santiago, and Catarina Barata. MMIST-ccRCC: A real world medical dataset for the development of multi-modal systems. In *Proceedings of Computer Vision and Pattern Recognition (CVPR)*, pages 2395–2403. IEEE, 2024. 1
- [66] M. F. Mridha, Akibur Rahman Prodeep, A. S.M.Morshedul Hoque, Md Rashedul Islam, Aklima Akter Lima, Muhammad Mohsin Kabir, Md Abdul Hamid, and Yutaka Watanobe. A comprehensive survey on the progress, process, and challenges of lung cancer detection and classification. *Journal of Healthcare Engineering*, 2022(1):5905230, 2022. 1
- [67] National Academies of Sciences, Engineering, and Medicine, Health and Medicine Division, Board on Population Health, Public Health Practice, Roundtable on Environmental Health Sciences, Research, and Medicine, E. Rusch, and R. Pool. *Principles and Obstacles for Sharing Data from Environmental Health Research: Workshop Summary*. National Academies Press, 2016. 1, 3
- [68] Sunday Olakanmi, Chithra Karunakaran, and Digvir Jayas. Applications of x-ray micro-computed tomography and small-angle x-ray scattering techniques in food systems: A concise review. *Journal of Food Engineering*, 342:111355, 2023. 2
- [69] Pawel Tomasz Pieta, Anders Bjorholm Dahl, Jeppe Revall Frisvad, Siavash Arjomand Bigdeli, and Anders Nymark Christensen. Feature-centered first order structure tensor scale-space in 2d and 3d. *Ieee Access*, 13:9766–9779, 2025. 8
- [70] Luc Salvo, Michel Suéry, Ariane Marmottant, Nathalie Limodin, and Dominique Bernard. 3D imaging in material science: Application of X-ray tomography. *Comptes Rendus Physique*, 11(9-10):641–649, 2010. 1
- [71] Mark Sandler, Andrew Howard, Menglong Zhu, Andrey Zhmoginov, and Liang Chieh Chen. MobileNetV2: Inverted residuals and linear bottlenecks. *Proceedings of Computer Vision and Pattern Recognition (CVPR)*, pages 4510–4520, 2018. 2, 5
- [72] Laura Schaad, Ruslan Hlushchuk, Sébastien Barré, Roberto Gianni-Barrera, David Haberthür, Andrea Banfi, and Valentin Djonov. Correlative imaging of the murine hind limb vasculature and muscle tissue by microCT and light microscopy. *Scientific Reports*, 7(1):41842, 2017. 2
- [73] Letitia Schoeman, Paul Williams, Anton du Plessis, and Marena Manley. X-ray micro-computed tomography ( $\mu$ CT) for non-destructive characterisation of food microstructure. *Trends in Food Science & Technology*, 47:10–24, 2016. 1
- [74] Arnaud Arindra Adiyoso Setio, Alberto Traverso, Thomas de Bel, Moira S. N. Berens, Cas van den Bogaard, Piergiorgio Cerello, Hao Chen, Qi Dou, Maria Evelina Fantacci, Bram Geurts, Robbert van der Gugten, Pheng Ann Heng, Bart Jansen, Michael M. J. de Kaste, Valentin Kottov, Jack Yu Hung Lin, Jeroen T. M. C. Manders, Alexander Sónora-Mengana, Juan Carlos García-Naranjo, Evgenia Papavasileiou, Mathias Prokop, Marco Saletta, Cornelia M. Schaefer-Prokop, Ernst T. Scholten, Luuk Scholten, Miranda M. Snoeren, Ernesto Lopez Torres, Jef Vandemeulebroucke, Nicole Walasek, Guido C. A. Zuidhof, Bram van Ginneken, and Colin Jacobs. Validation, comparison, and



- combination of algorithms for automatic detection of pulmonary nodules in computed tomography images: The LUNA16 challenge. *Medical Image Analysis*, 42:1–13, 2017. 1, 3, 8
- [75] Dinggang Shen, Guorong Wu, and Heung-II Suk. Deep learning in medical image analysis. *Annual Review of Biomedical Engineering*, 19(1):221–248, 2017. 1
- [76] Hongbin Shen, Steven Nutt, and David Hull. Direct observation and measurement of fiber architecture in short fiber-polymer composite foam through micro-CT imaging. *Composites Science and Technology*, 64(13-14):2113–2120, 2004. 2
- [77] Satya P. Singh, Lipo Wang, Sukrit Gupta, Haveesh Goli, Parasuraman Padmanabhan, and Balázs Gulyás. 3D deep learning on medical images: A review. *Sensors*, 20(18):1–24, 2020. 1
- [78] Mark D. Sutton. Tomographic techniques for the study of exceptionally preserved fossils. *Proceedings of the Royal Society B: Biological Sciences*, 275(1643):1587–1593, 2008. 1
- [79] Mingxing Tan and Quoc Le. EfficientNet: Rethinking model scaling for convolutional neural networks. In *Proceedings of the 36th International Conference on Machine Learning*, pages 6105–6114. PMLR, 2019. 2
- [80] Yucheng Tang, Dong Yang, Wenqi Li, Holger R. Roth, Bennett Landman, Daguang Xu, Vishwesh Nath, and Ali Hatamizadeh. Self-supervised pre-training of swin transformers for 3D medical image analysis. In *Proceedings of Computer Vision and Pattern Recognition (CVPR)*, pages 20698–20708. IEEE, 2022. 2
- [81] Kimberley M. Timmins, Irene C. van der Schaaf, Edwin Bennink, Ynte M. Ruijgrok, Xingle An, Michael Baumgartner, Pascal Bourdon, Riccardo De Feo, Tommaso Di Noto, Florian Dubost, Augusto Fava-Sanches, Xue Feng, Corentin Giroud, Inteneural Group, Minghui Hu, Paul F. Jaeger, Juhana Kaiponen, Michał Klimont, Yuexiang Li, Hongwei Li, Yi Lin, Timo Loehr, Jun Ma, Klaus H. Maier-Hein, Guillaume Marie, Bjoern Menze, Jonas Richiardi, Saïfeddine Rjiba, Dhaval Shah, Suprosanna Shit, Jussi Tohka, Thierry Urruty, Urszula Walińska, Xiaoping Yang, Yunqiao Yang, Yin Yin, Birgitta K. Velthuis, and Hugo J. Kuijff. Comparing methods of detecting and segmenting unruptured intracranial aneurysms on TOF-MRAS: The ADAM challenge. *NeuroImage*, 238:118216, 2021. 3
- [82] vit-pytorch maintainers and contributors. vit-pytorch. <https://github.com/lucidrains/vit-pytorch>, 2020. 5
- [83] C. L. Walsh, P. Tafforeau, W. L. Wagner, D. J. Jafree, A. Bellier, C. Werlein, M. P. Kühnel, E. Boller, S. Walker-Samuel, J. L. Robertus, D. A. Long, J. Jacob, S. Marussi, E. Brown, N. Holroyd, D. D. Jonigk, M. Ackermann, and P. D. Lee. Imaging intact human organs with local resolution of cellular structures using hierarchical phase-contrast tomography. *Nature Methods*, 18(12):1532–1541, 2021. 1
- [84] Zi Wang, Els Herremans, Siem Janssen, Dennis Cantre, Pieter Verboven, and Bart Nicolai. Visualizing 3D food microstructure using tomographic methods: Advantages and disadvantages. *Annual Review of Food Science and Technology*, 9(1):323–343, 2018. 2
- [85] Frederik Warburg, Soren Hauberg, Manuel Lopez-Antequera, Pau Gargallo, Yubin Kuang, and Javier Civera. Mapillary street-level sequences: A dataset for lifelong place recognition. In *Proceedings of Computer Vision and Pattern Recognition (CVPR)*, pages 2626–2635. IEEE, 2020. 3
- [86] Jakob Wasserthal, Hanns Christian Breit, Manfred T. Meyer, Maurice Pradella, Daniel Hinck, Alexander W. Sauter, Tobias Heye, Daniel T. Boll, Joshy Cyriac, Shan Yang, Michael Bach, and Martin Segeth. TotalSegmentator: Robust segmentation of 104 anatomic structures in CT images. *Radiology: Artificial Intelligence*, 5(5):e230024, 2023. 2
- [87] Xiongwei Wu, Xin Fu, Ying Liu, Ee-Peng Lim, Steven C.H. Hoi, and Qianru Sun. A large-scale benchmark for food image segmentation. In *Proceedings of the 29th ACM International Conference on Multimedia*, pages 506–515. ACM, 2021. 3
- [88] Han Xiao, Kashif Rasul, and Roland Vollgraf. Fashion-MNIST: a novel image dataset for benchmarking machine learning algorithms. arXiv:1708.07747 [cs.LG], 2017. 3
- [89] Enze Xie, Wenhai Wang, Zhiding Yu, Anima Anandkumar, Jose M. Alvarez, and Ping Luo. SegFormer: Simple and efficient design for semantic segmentation with transformers. *Advances in Neural Information Processing Systems 34 (neurips 2021)*, 34, 2021. 8
- [90] Saining Xie, Ross Girshick, Piotr Dollár, Zhuowen Tu, and Kaiming He. Aggregated residual transformations for deep neural networks. In *Proceedings of Computer Vision and Pattern Recognition (CVPR)*, pages 5987–5995. IEEE, 2017. 2
- [91] Yutong Xie, Jianpeng Zhang, Chunhua Shen, and Yong Xia. CoTr: Efficiently bridging CNN and transformer for 3D medical image segmentation. In *Medical Image Computing and Computer Assisted Intervention (MICCAI 2021)*, pages 171–180. Lecture Notes in Computer Science, Vol. 12903. Springer, 2021. 2, 8
- [92] Jiancheng Yang, Rui Shi, Donglai Wei, Zequan Liu, Lin Zhao, Bilian Ke, Hanspeter Pfister, and Bingbing Ni. MedMNIST v2 - a large-scale lightweight benchmark for 2d and 3d biomedical image classification. *Scientific Data*, 10(1), 2023. 3
- [93] Yefeng Zheng, David Liu, Bogdan Georgescu, Hien Nguyen, and Dorin Comaniciu. 3d deep learning for efficient and robust landmark detection in volumetric data. In *Medical Image Computing and Computer-Assisted Intervention (MICCAI)*, pages 565–572. Springer, 2015. 2
- [94] Hong Yu Zhou, Jiansen Guo, Yinghao Zhang, Xiaoguang Han, Lequan Yu, Liansheng Wang, and Yizhou Yu. nnFormer: Volumetric medical image segmentation via a 3D transformer. *IEEE Transactions on Image Processing*, 32: 4036–4045, 2023. 2
- [95] S. Kevin Zhou, Hayit Greenspan, Christos Davatzikos, James S. Duncan, Bram Van Ginneken, Anant Madabhushi, Jerry L. Prince, Daniel Rueckert, and Ronald M. Summers. A review of deep learning in medical imaging: Imaging

traits, technology trends, case studies with progress highlights, and future promises. *Proceedings of the IEEE*, 109(5):820–838, 2021. [1](#)

# MozzaVID: Mozzarella Volumetric Image Dataset

## Supplementary Material

### 8. Data visualization

#### 8.1. Scans

In Fig. 2, we introduce a set of example scan slices that illustrate the structural variability across the cheese samples. Subsequently, in Fig. 4c, we use slices from all scans to explore the representation learned by one of the models. To provide a clean and comprehensive overview of the variability, the same slices are arranged in an ordered grid in Fig. 8.

To further supplement the overview of the scanned samples, Fig. 9 showcases example slices from different fine-grained classes. These are organized into sets of six samples originating from the same cheese type, emphasizing their structural similarity and consequent increase in the complexity of the problem. However, it is important to note that a single 2D slice may not fully capture the sample’s structural characteristics, which are likely to be more effectively discerned through a full 3D representation.

#### 8.2. Metadata

In Sec. 3.1, we provide an overview of the metadata, including experimental design parameters, which are later visualized in a reduced form in Fig. 6.

The following PCA reduction was applied to three parameters: rotor speed, temperature, and additive type. The additive type is a categorical variable with three categories (None, CaCL2, and Citric Acid), to which a unique number is assigned. Each parameter is then normalized to maintain the confidentiality of the exact recipe. The resulting values are presented in Fig. 5, normalized to a zero mean and standard deviation of one.

### 9. Experiments

#### 9.1. Learning rate fine tuning

In Sec. 4, we outline the experimental design, including the investigated models and ablation studies. The training setup across all models is standardized to ensure a fair comparison of the models. However, certain hyperparameters should be fine-tuned to provide the most representative result. In this study, we focus on fine-tuning the learning rate, as it has the most significant impact on the consistency of model performance. Given the training and convergence constraints, fine-tuning was performed only for 2D models and 3D-fine models, while the remaining models used a default learning rate of  $10^{-4}$ .

Fine-tuning was conducted using the *Weights & Biases* parameter sweep over a log-uniform distribution in the

range  $lr \in \langle 10^{-2}, 10^{-6} \rangle$ , using the Bayesian optimization. Each model was tested with 30 hyperparameter variants, provided this could be achieved in 1 day of training. Otherwise, the number of tested variants was lowered to 15. The best configuration was selected based on the highest validation accuracy. The final learning rates for all models are listed in Tab. 4.

Although not all models underwent fine-tuning, those that did were also the ones most likely to benefit from it. The performance of the tested models tended to be more volatile and sensitive when trained on the smaller dataset variants. In the case of 2D-Small models, small learning rate changes often resulted in a 20 to 30 percentage point difference in accuracy, while for 2D-Large models, this difference was limited to approximately 1 to 5 percentage points. This behaviour suggests that the performance of 3D models, even without fine-tuning, remains representative and close to optimal. Furthermore, the strong performance of non-fine-tuned 3D models only strengthens the reported impact of the 3D representation and all conclusions drawn from it.

#### 9.2. PCA visualization

In Sec. 4.3, we introduce the outline of the learned representation analysis experiment. There, a PCA-based compression of the sample experimental design parameter space is described, together with an introduction of a colormap that is later used for the interpretation of the UMAP representation in Fig. 4b. The visualization of the PCA space, together with the colormap overlay, can be found in Fig. 6.

#### 9.3. Rotation ablation study

In Sec. 6.1, we discuss structure orientation as a potential source of bias, noting that while sample preparation and data augmentations largely mitigate this issue, it is not systematically addressed in the raw data. To evaluate the impact of volume orientation on the accuracy of the investigated models, we conducted an additional ablation study using a modified set of transforms.

This study focused on the ResNet50 model, given its consistent performance, and utilized the Base dataset as a central, representative example. Both 2D and 3D models were trained for coarse-grained and fine-grained tasks. Apart from the data augmentation, the training setup was exactly the same as in the original experiments.

The modified set of transforms included the following elements:

1. Normalization.
2. Random 90° rotation ( $p = 0.5$ ).

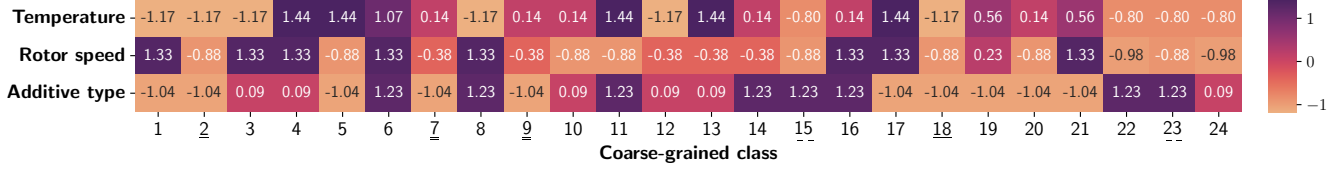


Figure 5. Overview of the variation in the normalized experimental design parameters in the first 24 cheese types (coarse-grained classes). Data for class 25 (Cagliata) is not available. Underlines highlight three pairs of cheese produced with the same set of parameters.

Table 4. Learning rate of the trained models on all investigated setups after fine-tuning. Base and Large 3D models were assigned a default learning rate due to the limited resources and slow convergence.

Granularity	Coarse						Fine			
	Small		Base		Large		Base		Large	
Split										
Dimensionality	2D	3D	2D	3D	2D	3D	2D	3D	2D	3D
ResNet50	$2.3 \times 10^{-3}$	$1.5 \times 10^{-3}$	$2.4 \times 10^{-3}$	$10^{-4}$	$4.0 \times 10^{-4}$	$10^{-4}$	$9.0 \times 10^{-4}$	$10^{-4}$	$3.3 \times 10^{-4}$	$10^{-4}$
MobileNetV2	$4.2 \times 10^{-3}$	$5.8 \times 10^{-3}$	$4.9 \times 10^{-3}$	$10^{-4}$	$4.6 \times 10^{-4}$	$10^{-4}$	$1.9 \times 10^{-3}$	$10^{-4}$	$6.0 \times 10^{-4}$	$10^{-4}$
ConvNeXt-S	$2.2 \times 10^{-3}$	$4.0 \times 10^{-4}$	$8.8 \times 10^{-4}$	$10^{-4}$	$9.4 \times 10^{-4}$	$10^{-4}$	$1.3 \times 10^{-3}$	$10^{-4}$	$1.0 \times 10^{-3}$	$10^{-4}$
ViT-B/16	$3.0 \times 10^{-5}$	$2.7 \times 10^{-4}$	$4.8 \times 10^{-5}$	$10^{-4}$	$1.3 \times 10^{-4}$	$10^{-4}$	$3.4 \times 10^{-6}$	$10^{-4}$	$5.0 \times 10^{-5}$	$10^{-4}$
Swin-S	$1.6 \times 10^{-4}$	$4.4 \times 10^{-6}$	$1.3 \times 10^{-5}$	$10^{-4}$	$2.4 \times 10^{-4}$	$10^{-4}$	$2.4 \times 10^{-6}$	$10^{-4}$	$8.8 \times 10^{-5}$	$10^{-4}$

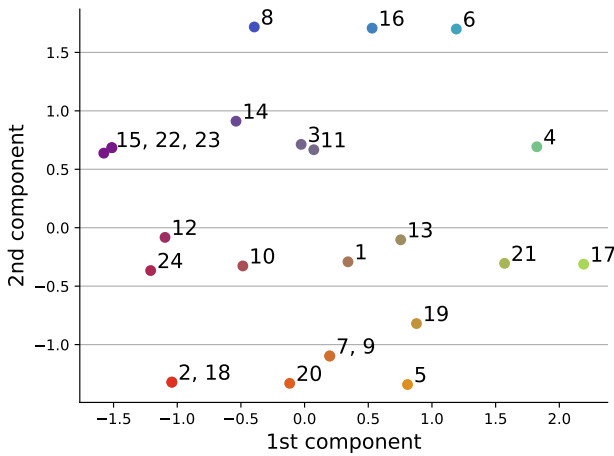


Figure 6. PCA of the experimental design parameters used to define the mozzarella cheese variations. Class 25 (Cagliata cheese) is omitted – it was prepared separately, and its exact recipe is not available. Coloring of the points serves as a basis for visual analysis of structural similarities learned by the models (Fig. 4b).

3. Random flipping in X and Y axis ( $p = 0.5$ ).
  4. Random rotation in a  $-30^\circ$  to  $30^\circ$  range ( $p = 0.5$ ).
- Elements 1 and 3 were retained from the original pipeline. The combined set of transforms covers most of the possible structure orientations while minimizing information loss at the most extreme angles.

The results of the study (Tab. 5) suggest that volume orientation does not exhibit a clear or consistent impact on training accuracy. The coarse-grained models seem to perform better or similarly with the new setup, suggesting a

Table 5. Results of rotation ablation study using the ResNet50 model and the Base dataset instance. Reference results copied from Tab. 3.

Granularity	Coarse		Fine	
	2D	3D	2D	3D
Reference	0.781	0.973	0.563	0.683
With rotations	0.830	0.971	0.498	0.643

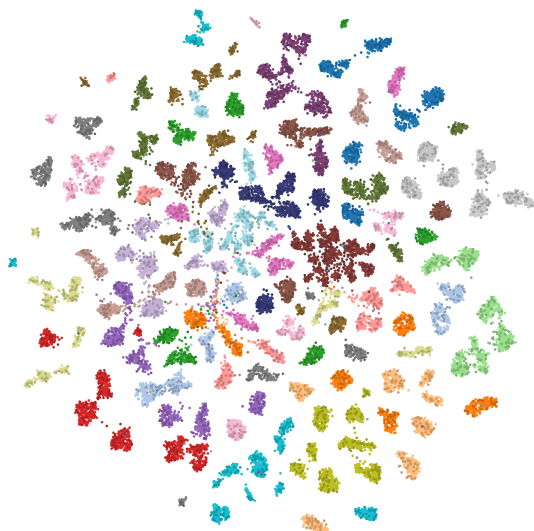
positive influence of data augmentation on generalization. The impact on fine-grained models is more negative compared to coarse-grained models, which may be due to fine-grained models relying more heavily on structure orientation, as each sample (fine-grained class) is cut in a single direction, with variation introduced only through data augmentation. However, this effect is not significant enough to undermine the validity of the dataset or the presented results.

#### 9.4. Fine-grained model UMAP

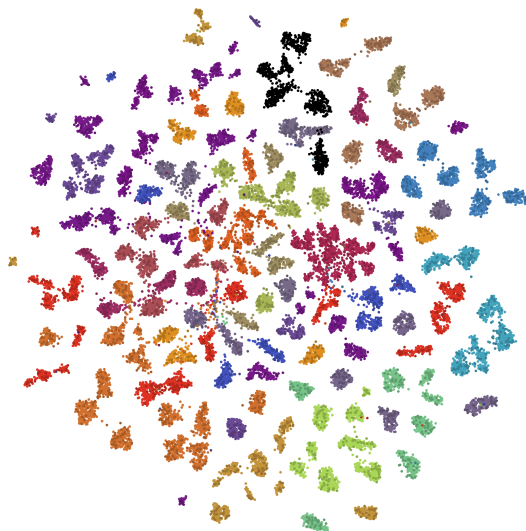
A similar experiment to the one described in 4.3 and visualized in 4 was conducted using the best-performing fine-grained model. The resulting UMAPs are shown in Fig. 7, though the slice-based visualization is omitted here for readability. The colormaps remain consistent with those used in the coarse-grained analysis.

Despite a different target, in most cases the network still groups samples from the same coarse-grained class in close proximity (Fig. 7a). This behavior indicates that structural similarities within these samples significantly influence the





(a) Clusters colored by class.



(b) Clusters colored by experimental design PCA color space. Class 25 is colored black.

Figure 7. UMAP generated from second-to-last layer feature representations of the best-performing model in the fine-grained classification task (ResNet50 trained on the Large dataset). Reduction parameters: `n_neighbors=30`, `min_dist=0.8`.

embedding space constructed by the model. As shown in Fig. 7b, the alignment with PCA space appears similar or even stronger compared to the coarse-grained model. The UMAP reveals four distinct zones with purple samples in the top-left, orange/red in the bottom-left, green in the bottom-right, and blue on the right. While some exceptions are present, these can often be explained by structural properties that deviate from the PCA parameters, as discussed in Sec. 5.2. This layout suggests that the fine-grained model captures a more nuanced representation of the structural variability, which may result from the need to detect subtler differences between samples and the absence of regularizing constraints imposed by the 25 coarse-grained classes.

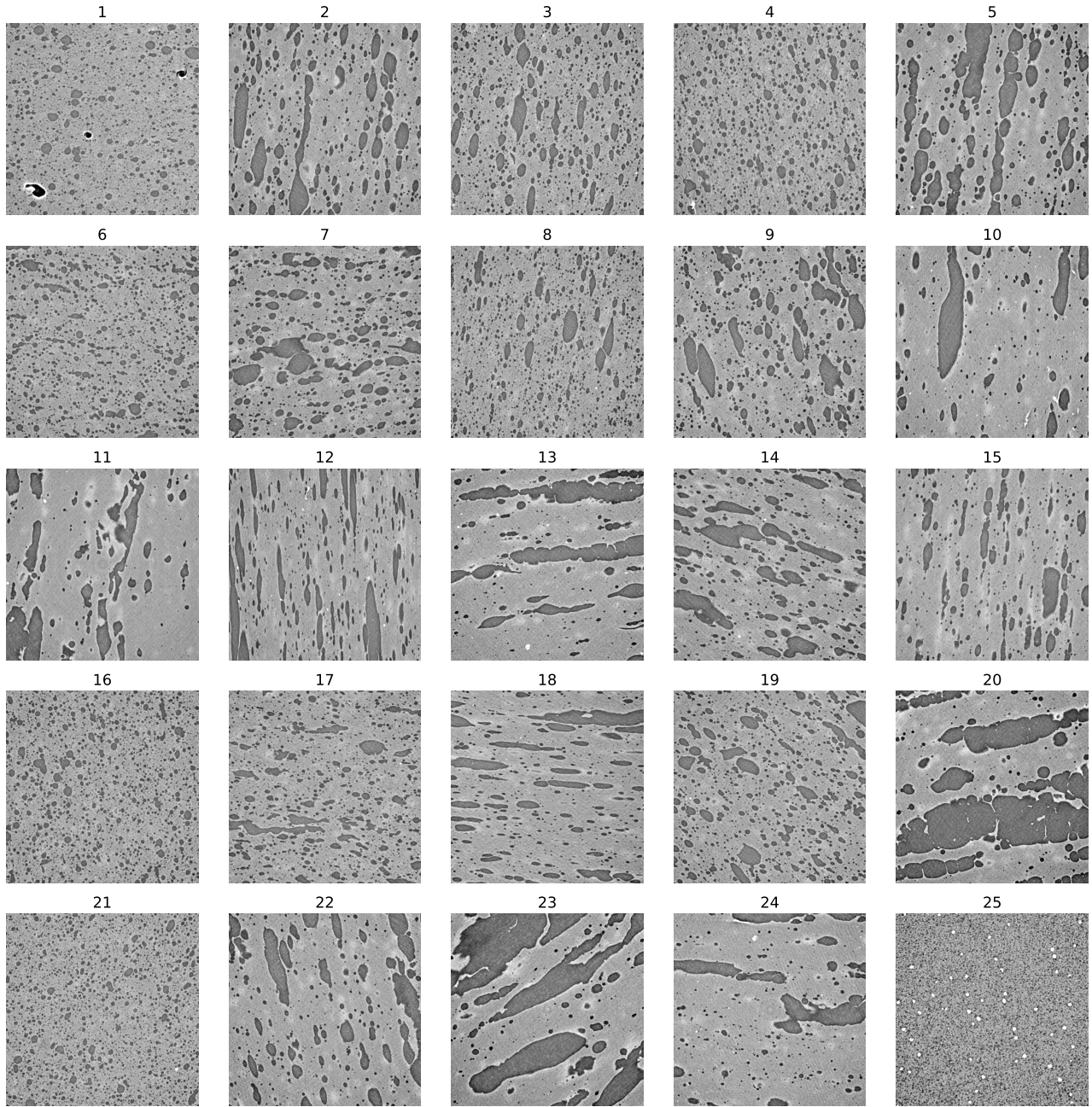


Figure 8. Overview of slices from each cheese type, forming the 25 coarse-grained classes.

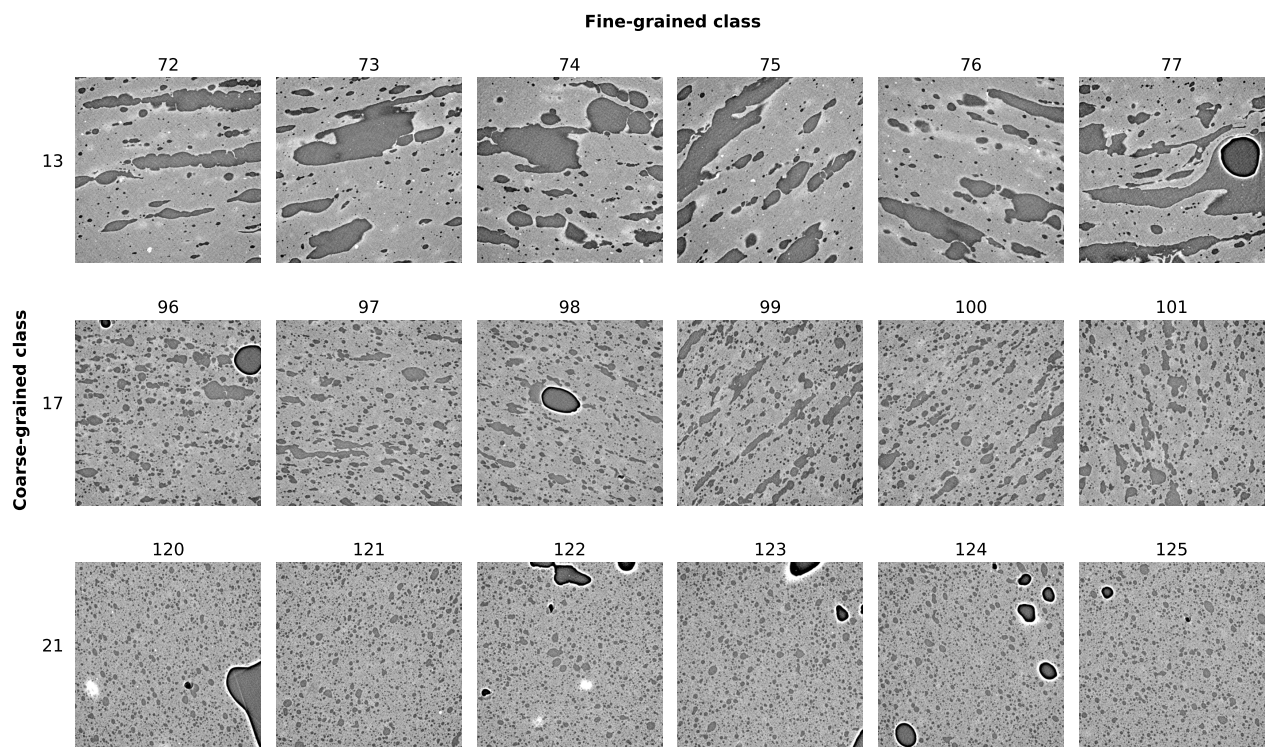


Figure 9. Example slices from the fine-grained classes. Each row represents a set of six samples from one cheese type (coarse-grained class), forming six consecutive fine-grained classes.